Journal of Hydroscience and Hydraulic Engineering
Vol. 29, No.1 May, 2011, 107-121



# FLOW STRUCTURES AT A SMALL ANGLED CONFLUENCE IN FIXED AND MOVABLE BEDS

By

Ichiro Fujita

Department of Civil Engineering, Graduate School of Engineering, Kobe University, Nada, Kobe, Japan

Ken Kadotani

Ph.D student, Department of Civil Engineering, Graduate School of Engineering, Kobe University, Nada, Kobe, Japan

and

Toshifumi Tanaka

Undergraduate student, Department of Civil Engineering, Graduate School of Engineering, Kobe University, Nada, Kobe, Japan

## SYNOPSIS

It is thought that combining flows at open-channel confluences with an alluvial bed induce local scour along the mixing zone for a relatively large confluence angle, and that the scour hole is generated by a pair of secondary flows developed along the dividing streamline. However, experimental examinations of three-dimensional flow structures as well as bed variations have rarely been conducted because of difficulties in performing detailed experiments under such complicated flow situations. In this research, to examine the occurrence of the secondary flows even under the condition of a flow with a small confluence angle, a fixed bed and movable bed experiments are conducted for the confluence angle of fifteen degrees without changing the total width of the channels before and after the junction point. In the fixed bed experiment, we measured three-dimensional flow fields by means of a sophisticated PIV method. In the movable bed experiment, the surface flow velocity distributions were measured by PIV while the bathymetries were measured by means of photogrammetric measurement technique. We made it clear that a couple of secondary flows are actually generated at the confluence through detailed velocity measurements in the fixed bed experiment. Moreover, the movable bed experiment revealed that a longitudinal local scour is developed along the dividing line even at the confluence with a small confluence angle.

## INTRODUCTION

Flows at an open channel confluence generate various types of flow structures such as developments of free shear layer between the combining flows and a pair of secondary flows along the mixing layer (Weerakoon and Tamai (1), Fujita and Komura (2)). The flow structure becomes more complicated for a relatively large confluence angle (Fujita and Komura (3), Fujita et al.(4), Chang et al.(5), Fujita and Komura (6)), in which a large-scale unsteady separation zone is generated just downstream of the junction point. In the case of a movable bed confluence, a local scour along the mixing layer tends to occur due to the secondary flows. With respect to numerical simulations of confluence flows, Weerakoon and Tamai (7) calculated a three-dimensional flow by using a body-fitted coordinates by k-e turbulence model. Bradbrook et al. (8) simulated the time-averaged three-dimensional flow structures for various types of confluences. Recently, Miyawaki et al. (9) has performed a three-dimensional large eddy simulation for a small scale natural river confluence subjected to a local scour which showed the occurrence of a pair of spiral flows near the bed. However, most of the previous studies revealed no detailed comparison with measured data as they were not easily available in the experiments or in field conditions. Moreover, the cases of any secondary flows for a small confluence angle has not yet verified yet and at the same time its effect on alluvial bed is not clearly understood. Therefore, firstly the authors conducted measurements of a confluence flow with a relatively small angle of fifteen degrees under flat fixed-bed conditions. Secondly, experiments for a movable bed condition using the same channel are executed to examine the generation of local scour at the confluence. In the fixed-bed experiments, three-dimensional flow structure at the confluence was measured by means of the particle image velocimetry (PIV) at multiple vertical and horizontal cross sections by shifting the position of a laser light sheet (LLS); whereas in the movable-bed experiments only the water surface flow was measured by PIV as it is difficult to measure the internal flow with LLS. Furthermore, the channel bed bathymetry was measured using a photogrammetric technique after a dynamic equilibrium condition was established. Based on findings from fixed- and movable-bed experiments, the structure of the secondary flow at the confluence will be discussed in detail in the following sections.

## EXPERIMENTAL SETUP

The flume which was used in the experiments is depicted in Fig.1. Discharges in the main and tributary channels were supplied with two independent pumps submerged in the downstream water tank and were controlled by valves and measured by means of electromagnetic flow meters. The confluence angle was set at 15 degrees, which was considered small enough not to generate a large-scale separation zone just downstream of the tributary channel. The width of the upstream main channel $B_1$ and the tributary channel $B_2$ is 0.15m, the width of the downstream main channel $B_3$ is 0.3m, and the bed slope is 1/1000 for the fixed bed experiment. The main and tributary channels were setup vertically within the area of 0.6m by 4.0m by using several wooden attachments shown in Fig.1. The experimental conditions for the fixed- and movable-bed are shown in Table 1 and Table 2, respectively. Here, $h$ is the water depth, $Fr$ the Froude number and $Re$ the Reynolds number. The subscripts 1, 2 and 3 stand for the parameters at $x$=-5cm in the upstream main channel, at $x$=-5cm in the tributary channel and at $x$=35cm in the downstream main channel, respectively. The discharge ratio $Q_r$ is defined by $Q_2/Q_3$.

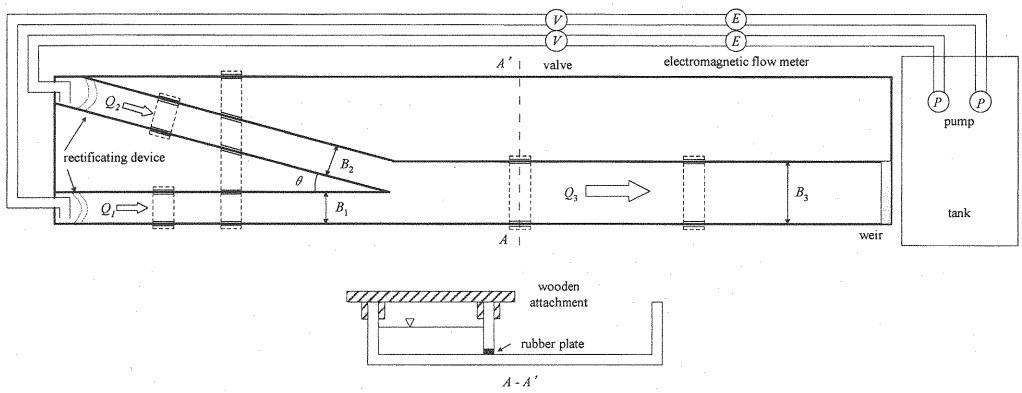


Fig.1 Confluence flume used for the experiment

Table 1 Conditions for fixed bed experiment

| CASE | $Q_1$ l/s | $Q_2$ l/s | $Q_3$ l/s | $Q_r$ | $h$ cm | $Fr_1$ | $Fr_2$ | $Fr_3$ |
|---|---|---|---|---|---|---|---|---|
| F01 | 0.902 | 0.602 | 1.503 | 0.4 | 4 | 0.24 | 0.16 | 0.2 |
| F02 | 0.752 | 0.752 | | 0.5 | | 0.20 | 0.20 | |
| F03 | 0.602 | 0.902 | | 0.6 | | 0.16 | 0.24 | |
| F04 | 1.803 | 0.902 | 3.007 | 0.4 | | 0.48 | 0.32 | 0.4 |
| F05 | 1.503 | 1.503 | | 0.5 | | 0.40 | 0.40 | |
| F06 | 0.902 | 1.803 | | 0.6 | | 0.32 | 0.48 | |

Table 2 Conditions for movable bed experiment

| CASE | $Q_3$ l/s | $Q_r$ | $Re_3$ | $h_1$ cm | $h_2$ cm | $h_3$ cm | $Fr_1$ | $Fr_2$ | $Fr_3$ |
|---|---|---|---|---|---|---|---|---|---|
| M01 | 1.0 | 0.4 | 3333 | 1.6 | 1.5 | 1.8 | 0.61 | 0.47 | 0.44 |
| M02 | | 0.5 | | 1.6 | 1.4 | 1.8 | 0.54 | 0.64 | 0.43 |
| M03 | | 0.6 | | 1.4 | 1.7 | 1.6 | 0.47 | 0.56 | 0.70 |
| M04 | 2.0 | 0.4 | 6666 | 3.3 | 2.9 | 3.2 | 0.42 | 0.34 | 0.37 |
| M05 | | 0.5 | | 3.0 | 2.9 | 2.9 | 0.40 | 0.44 | 0.44 |
| M06 | | 0.6 | | 2.5 | 3.6 | 3.2 | 0.44 | 0.37 | 0.38 |
| M07 | 3.0 | 0.4 | 10000 | 4.7 | 3.8 | 4.2 | 0.38 | 0.34 | 0.37 |
| M08 | | 0.5 | | 4.1 | 4.2 | 4.2 | 0.39 | 0.36 | 0.37 |
| M09 | | 0.6 | | 3.9 | 4.8 | 4.0 | 0.34 | 0.37 | 0.40 |

The values of $h$ and $Fr$ are calculated at $x$=-5cm for $h_1$, $h_2$, $Fr_1$, and $Fr_2$ and at $x$=35cm for $h_3$ and $Fr_3$

In the fixed bed experiment, horizontal and longitudinal planes were visualized using LLS by shifting its location vertically or transversely as shown in Fig.2. The LLS is generated using a rod-type cylindrical lens connected to an argon ion laser by an optical fiber cable. The visualized flow was captured with a high-speed camera at 200 fps for a horizontal plane and at 500 fps for a vertical plane. In the horizontal measurements, nine horizontal sections between $z$=0.2 cm and 3.8 cm are captured with an image size of 1024 by 992 pixels for about ten seconds, while in the vertical measurements, fifteen

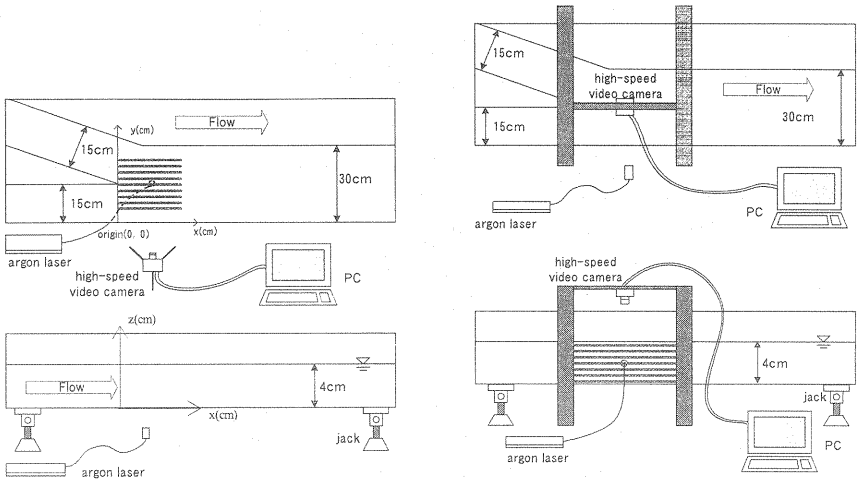


(a) Setup for vertical measurements (b) Setup for horizontal

Fig.2 Setups for PIV measurements

longitudinal vertical sections between $y$=6cm and 24cm are captured with an image size of 1024 by 496 pixels for about twenty seconds. Here, $y$ is the transverse coordinate measured from the right side wall and $z$ is the vertical coordinate from the channel bottom. The reason for using a higher image sampling rate in the vertical measurement is to capture out-of-plane movements of tracer particles as much as possible where tributary flow obliquely crosses the LLS. The captured images were analyzed by a higher-order optical flow method of particle image velocimetry (PIV) developed by the authors with a template size of 30 by 30 pixels. The vector spacing is 30 pixels, about 1cm in physical scale in the horizontal measurement and 10 pixels, about 0.17cm in the vertical measurement. With the above multiple-plane measurements, three-dimensional flow information within a volume of $x$=0~15cm, $y$=6~24cm and $z$=0~4cm can be reconstructed.

In the movable bed experiment, anthracite particles with a mean diameter of 0.6mm and a specific gravity of 1.4 were supplied in the channel with a thickness of about three centimeters. This particle material was selected so that appreciable bed variations would take place under a reduced shearing stress in a small-scale channel. The experiment was started from an initial flat bed condition while supplying anthracite particles from the upstream end of each channel. The bed material is supplied manually so that the bed level of each upstream reach is kept almost constant. Water surface velocity distributions were measured by PIV at a sampling rate of 100 fps using floating tracer particles with a mean diameter of 20μm. The measurement was conducted when the bed reached a dynamic equilibrium condition. In addition, the bed bathymetry was measured using a photogrammetric technique from a pair of still digital images after gradually draining the water from the channel, in which a thin wood stick is used as a ground control point (GCP).

## FIXED BED EXPERIMENT

The general feature of the flow near the bottom at a confluence can be visualized by the dye injection method devised by Kadotani et al. (10). In this method, viscous white dye is pasted across the channel bottom with a needle as a line and the flow nearest to the bottom is visualized by the dye gradually stretched in the downstream direction. Thus the bottom

streaklines can be clearly visualized as a white pattern. An example of visualized bottom streaklines starting from the section at $x$=0cm is shown in Fig.3(a). It is evident that the bottom streaklines steering around the dark wedge-shaped zone appeared in the center of the channel. In addition, Fig.3(b) shows the bottom streaklines within the wedge-shaped zone, indicating the streaklines tend to diverge in the opposite direction. These findings suggest that some type of descending flow was generated along the interface between the two joining flows even when the confluence angle is relatively small.

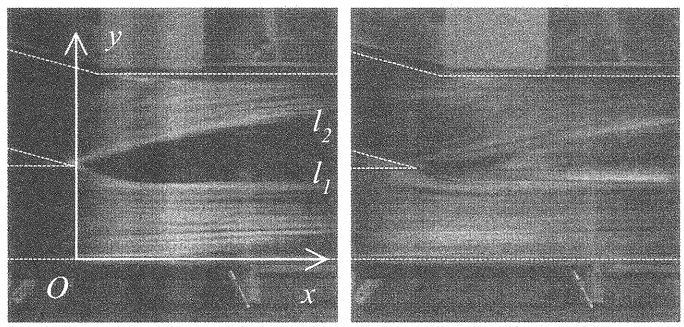


(a) viscous dye injected along y axis (b) viscous dye injected within wedge-like zone

Fig.3 Bottom streaklines visualized by injecting viscous white dye on the bottom which extends in the downstream direction being adhered to the bed

In order to examine the general structure of the flow at the confluence, horizontal velocity distributions near the bottom at z=0.2cm and close to the water surface at z=3.8cm are compared in Fig.4. Here, the contour plot illustrates the distribution of transverse velocity component, $v$, to show the direction of the flow more clearly. As shown in Fig.4(a)(c)(e), although the discharge ratio is different from case to case, the transverse velocity component near the bottom indicates a negative value downstream of the upstream main channel for a range of $y$ less than 15cm, while it takes positive value in the region nearer to the tributary channel for $y$ greater than 15cm. On the other hand, the flow near the water surface was quite different from the near-bottom flow as illustrated in Fig.4(b)(d)(f), in which most of the transverse velocity components showed a negative value. This indicates that the near-surface flow is mainly subject to the inertia of the tributary stream directed towards the main flow in an angle of negative direction. This feature intensified as the discharge ratio increases. The above flow features in terms of the transverse flow direction suggest that a large-scale flow structure is generated at the confluence region even for a small confluence angle. Furthermore, the local flow deceleration along the interface, or the dividing line, between the merging flows make the flow structure more complicated. In order to make clear the effect of the discharge ratio from another aspect, near-surface pathlines are plotted in Fig.5 by using the same PIV data as in Fig.4, except that the number of vectors used for plotting is much larger than that in Fig.4. It is apparent that pathlines tend to diverge along the dividing line as the discharge ratio increases, suggesting a generation of upwelling flow for the increase of tributary flow.

To examine the vertical structure at a confluence, velocity distributions at several streamwise vertical cross sections for the case of F02 were compared in Fig.6. The contour map in the figure denotes the distribution of vertical velocity components. Despite the relatively small lateral spacing of 1/30 of the main channel width, vertical velocity distributions

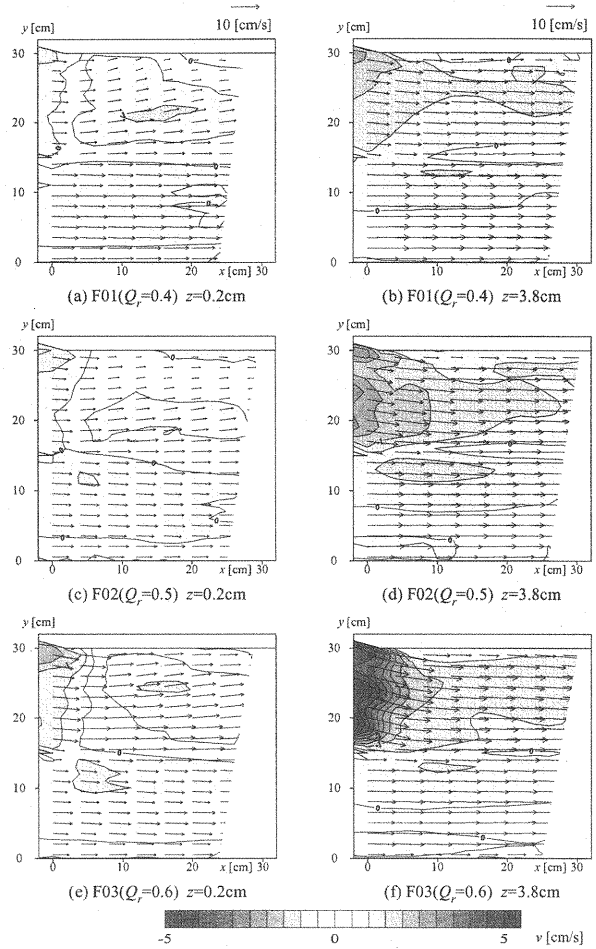


Fig.4 Velocity distribution in horizontal planes

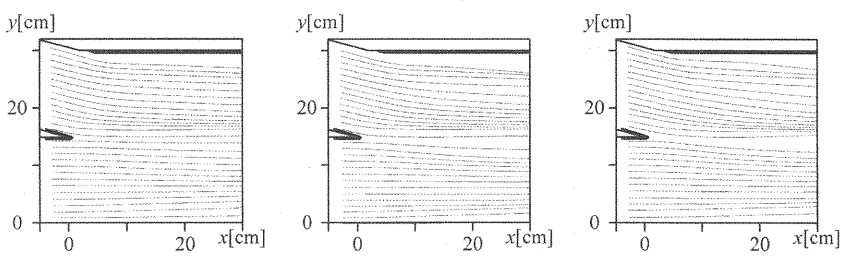


Fig.5 Near-surface pathlines at a confluence ($z$=3.8cm)

differ significantly from section to section, especially at $y$=14cm where intense upward flow was observed near the water surface. It should be noted that the maximum upward flow appeared just beneath the water surface at this section, which roughly corresponds to the dividing line between the converging flows. Such an upward flow was supplied from the upper art of the tributary flow running against the main stream. Conversely, the other sections are dominated by the

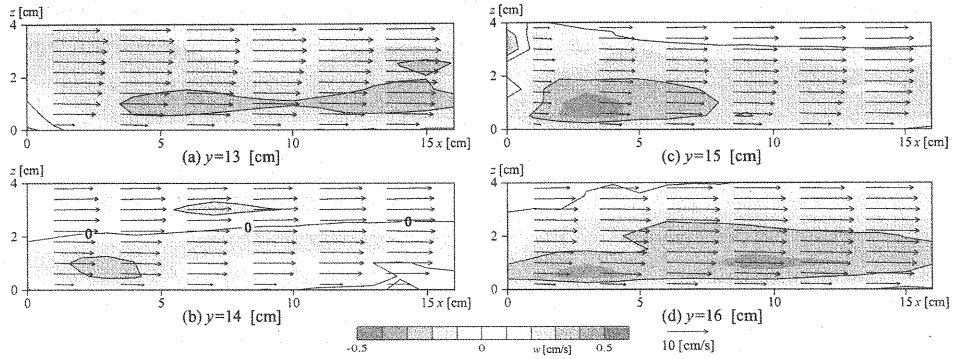


Fig.6 Velocity distribution in longitudinal vertical sections (case F02)

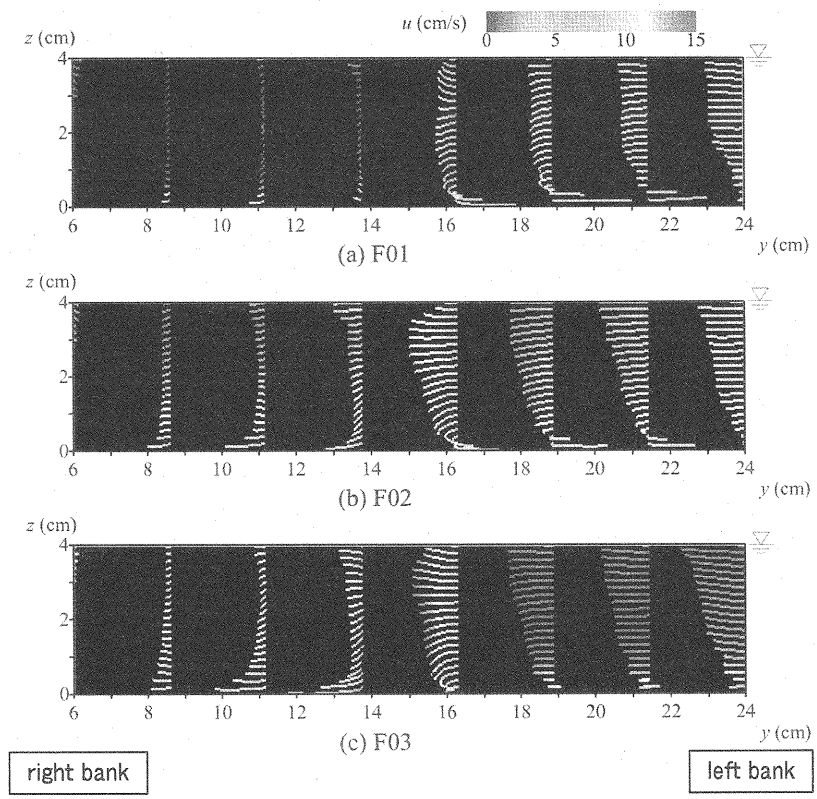


Fig.7 Three dimensional streamlines viewed from a downstream section for fixed bed experiments

downward flow in most of the region which increases nearer to the bottom and extends in the downstream direction as shown in Fig.6(a) and Fig.6(d). The cross-sectional data presented previously all suggest a generation of a large-scale secondary flow at the confluence.

In order to figure out the three-dimensional flow structure at a confluence, three-dimensional pathlines are drawn in Fig.7 by using the horizontal and vertical data for the cases F01, F02 and F03. In Fig.7 the pathlines are viewed upstream from downstream side of the measurement volume without any perspective treatment of the view. The direction of pathlines can be detected from the direction of a line segment starting from the same horizontal coordinate at various heights. The color of the line segment indicates the magnitude of velocity component in the streamwise direction. The pathlines on the right of each figure illustrate the secondary flow pattern in terms of the tributary channel, while the other side shows the pattern in the main channel. It is evident that general pattern of the secondary flow is similar to each other regardless of the discharge ratio; i.e. downward and diverging flow near the bottom and upward flow near the water surface in the channel center at around $y$=15cm. The downward flow feature accounts for the generation of wedge-like pattern of bottom streaklines previously explained in Fig.3 and the upward flow corresponds to the boiling phenomena observed in the channel center during the experiment. However, for the smaller discharge ratio the main stream pattern seems to be insensitive to the tributary flow as shown in Fig.7(a), but for the larger discharge ratios the main flow pattern is subject to the inflow from the tributary channel as indicated in Fig.7(b) and Fig.7(b). The unexpected characteristics with respect to the secondary flow pattern indicate that the defection point of the secondary flow is very close to the wall and that a skewed spiral flow is generated at the confluence, which is different from the previous image in which a pair of circular spiral flows contributes to the three-dimensional flow structure there.

In order to clarify the bottom shear stress distributions at the confluence, we calculated the streamwise and lateral shear velocity distributions by using the following two-layer model proposed by Werner and Wengel (11):

$$\bar{u}/u^* = y^+ \qquad (y^+ < 11.81) \tag{1}$$

$$\bar{u}/u^* = 8.3(y^+)^{1/7} \qquad (y^+ > 11.81) \tag{2}$$

where $\bar{u}$ is either streamwise or lateral mean velocity measured at $z$=0.2cm, $u^*$ is the shear velocity, $\nu$ is the kinematic viscosity and $y^+ = u^* y/\nu$. The calculated results are shown in Fig.8. It can clearly be seen that the streamwise shear stress distribution downstream of the tributary channel increases with the discharge ratio. In the case F01, the transverse distribution displays local peak just downstream of the junction. In the case F02 shown in Fig.8(b), the incoming flow velocities from tributary and upstream main channels are almost identical and indicate more uniform shear stress distributions than the case F01, but even in this case, there appears to be a local peak of streamwise shear stress at the confluence region along the interface of the incoming flows. The above increase of the streamwise shear stresses can be attributed to the effect of the local secondary flow near the bottom. Though not as clear as in the previous cases, case F03 displays a similar feature of the local shear stress distribution near the interface region as well. For a better understanding of general flow feature, dividing streamlines passing through the center of the local peak region of shear stresses are indicated as black dotted lines in Fig.8(a)-(c). These lines correspond to the center of the wedge-like zone shown in Fig.3. Meanwhile, the lateral components of the shear stress distribution are shown in Fig.8(d)-(f). The local peak zones are generated clearly on both sides of the dividing streamline with its value larger in the near-tributary area, suggesting that the bed material could be transferred more significantly towards the tributary side and thus a longitudinal local scour could be produced when the channel bed had been replaced with a movable bed.

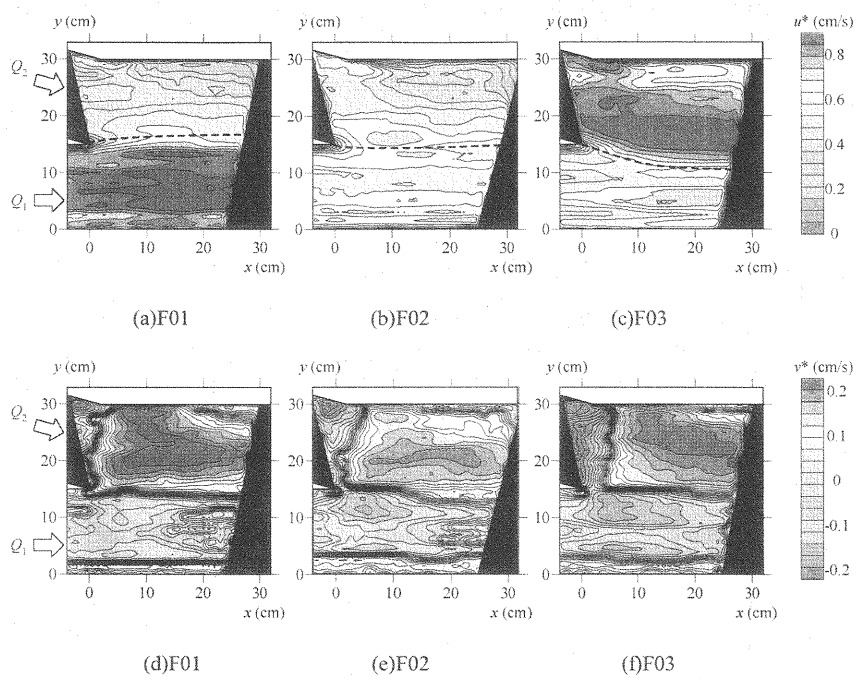


Fig.8 Shear velocity distributions in streamwise direction (a)-(c) and lateral direction (d)-(f) calculated from PIV data at $z$=0.2cm

## MOVABLE BED EXPERIMENT

After conducting the fixed bed experiments, the channel bed was covered with anthracite particles with a thickness of about 3cm keeping the same confluence configuration. The hydraulic conditions for the experiments are indicated previously in Table 1. Starting from flat bed conditions, measurements of velocity distribution at the water surface by PIV were carried out after the bed seems to reach a dynamic equilibrium condition by visual inspection. Subsequently, bathymetry measurement by photogrammetric method using a digital camera was conducted after carefully draining the water from the channel.

Fig.9 compares surface pathlines and divergence distributions for the same discharge ratio with different discharge and water depth. It is evident that the pathline along the side wall of the tributary channel separates at the edge of the channel corner and deviates farther from the side wall, especially for the larger water depth as shown in Fig.9(c). All of these deviations are greater than the fixed-bed cases already shown in Fig.5. This difference can be attributed to the change of the flow structure after the bed variation at the confluence. However, the surface structure differs slightly depending on the water depth; i.e. in the case of M02 with the smallest water depth the pathlines tend to converge towards the dividing line as shown in Fig.9(a), while in other cases they tend to diverge along the dividing line accompanying two converging zones on its both sides as illustrated in Fig.9(b) and (c). Moreover, since there is no supply of water at the water surface from above, the upwelling flow might be generated at the region with positive divergence value and sink flow at the negative divergence region. Fig.9(d-f) present such a surface flow feature despite there appears slight difference in the divergence values. Such differences in surface flow patterns can be accounted for by the relative scale of secondary spiral flow to the water depth; i.e. for a shallower case the effect of the secondary flow extends to the water surface

generating a sink flow region along the dividing line. On the other hand, for a relatively deeper case, as the effect of the secondary spiral flow is restricted to the near bottom field, the near water-surface field tends to show a feature similar to the fixed-bed secondary flow which accompanies upwelling flow along the dividing line.

Fig.10 shows the bed bathymetries measured at an equilibrium condition for different hydraulic conditions. It is

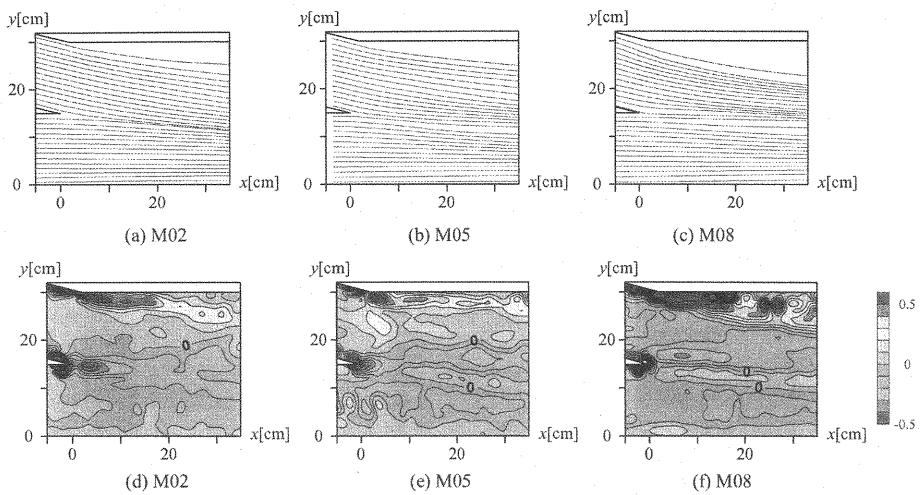


Fig.9 Surface pathlines and divergence distributions for movable bed experiments

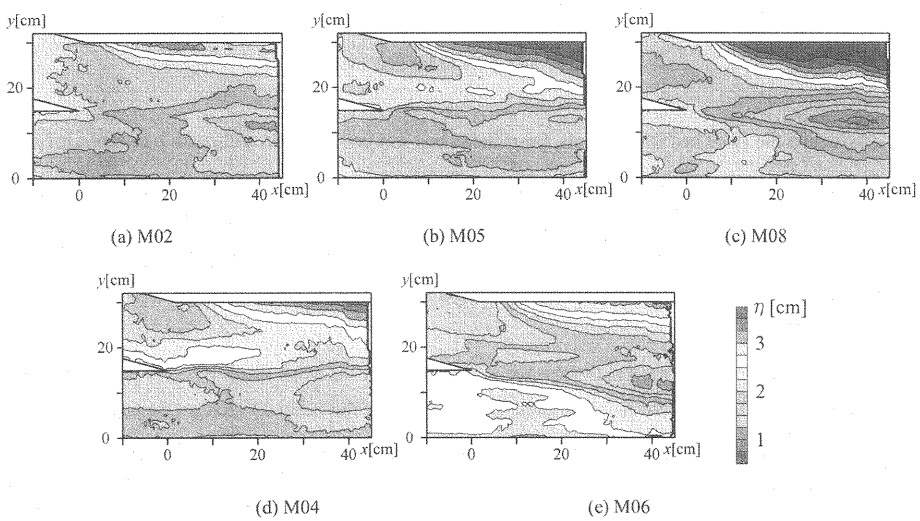


Fig.10 Comparison of final bathymetry for movable bed experiments

apparent that there appears a deposition of bed load downstream of the tributary channel and a local scour in the center of the channel at the confluence region even under the condition of small confluence angle. This feature of significant deposition of bed load had not been expected beforehand because large-scale horizontal vortices which should attract bed particles were not recognized clearly in the surface flow visualization. However, in reality a relatively larger pressure gradient in a lateral direction attracts bed particles behind the corner of the channel and gradually deposits them on the tributary side of the channel. This tendency is pronounced as the depth of water increases even for the same discharge

ratio as shown in Fig.10(a)-(c). On the other hand, Fig.10(d) and Fig.10(e) compares the effect of discharge ratio for the same total discharge, indicating that the channel bed is degraded where a larger discharge passes through the channel, e.g., the bed elevation becomes lower along the channel course of the tributary flow when the discharge ratio is relatively large as indicated in Fig.10(e). As for the local scour generation, a visual inspection of particle movements suggests that they tend to travel on both side of the scoured zone. This indicates a pair of spiral secondary flow is generated along the scour hole while keeping the bed close to the critical tractive force condition. It should be noted that the depth of the scour hole increases with the water depth for the same discharge ratio as shown in Fig.10(a-c), which indicates that the effect of the spiral secondary flows becomes relatively large with the increase of vertical space that allows the growth of the secondary flow. Fig.11 compares the maximum scour depth normalized by the average water depth at $x$=40cm which roughly corresponds to the location of the maximum scour hole. Allowing for the scattering of the data, the normalized maximum scour depth varies between 0.3 and 0.4 independent of the Reynolds number and discharge ratio within the range of the present experiments. This indicates that the local scour depth at a confluence depends mainly on the water depth, which is similar to the local scour behind a pier.

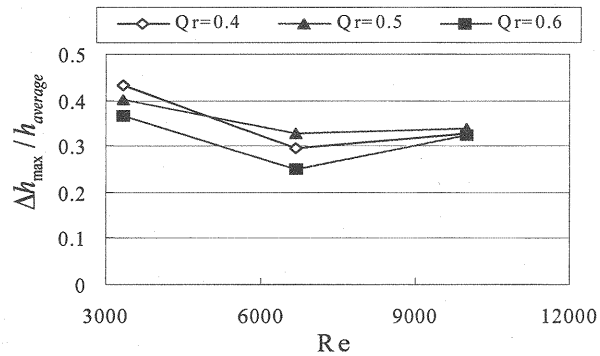


Fig.11 Comparison of relative maximum scour ($h_{max}$ -$h_{average}$)/ $h_{average}$ at a cross section $x$=40cm

## DISCUSSIONS

The secondary flow distributions in fixed-bed experiment and the lateral bed elevations in movable-bed experiment at $x$=15cm are compared in Fig.12. Fig.12(a)-(c) clearly indicate the generation of downward flow near the bottom in the center of the channel. Its location corresponds to a dividing line between the two joining flows, which in line with the observation previously noted in terms of Fig.7(a)-(c). It is apparent that the intensity of the secondary flow which is generated on the tributary side increases with discharge ratio and in the center of the channel part of the secondary flow near the water surface is deflected upward inducing an upwelling flow. When we compare the fixed-bed result of F05 and the movable-bed result of M08 with almost the same incoming discharges and water depths, we can assume that the secondary flow structure in M08 is similar to F05 since the location of the local scour in M08 agrees with the dividing line at about $x$=15cm, there also appears an upwelling flow in the center of the channel. On the other hand, the movable-bed cases of M07 and M09 should have the same flow structure as F04 and F06 respectively at the initial condition; however, as the degradation or aggradation of bed elevation takes place in the joining channels before reaching the equilibrium status, the incoming mean velocities becomes almost identical with each other. Therefore, the general flow structures of M07

and M09 may tend to become somewhat similar to the case of F05 in which the incoming flow velocities are almost identical, except the effect of the change in bathymetry.

Finally, from the experimental findings and observation of bed variation at the confluence, the general process of the bed evolution starting from flat-bed condition with the same incoming velocities is illustrated in Fig.13. Initially, as in the case of fixed bed experiment, a pair of spiral secondary flows is generated within the wedge-like zone along the dividing

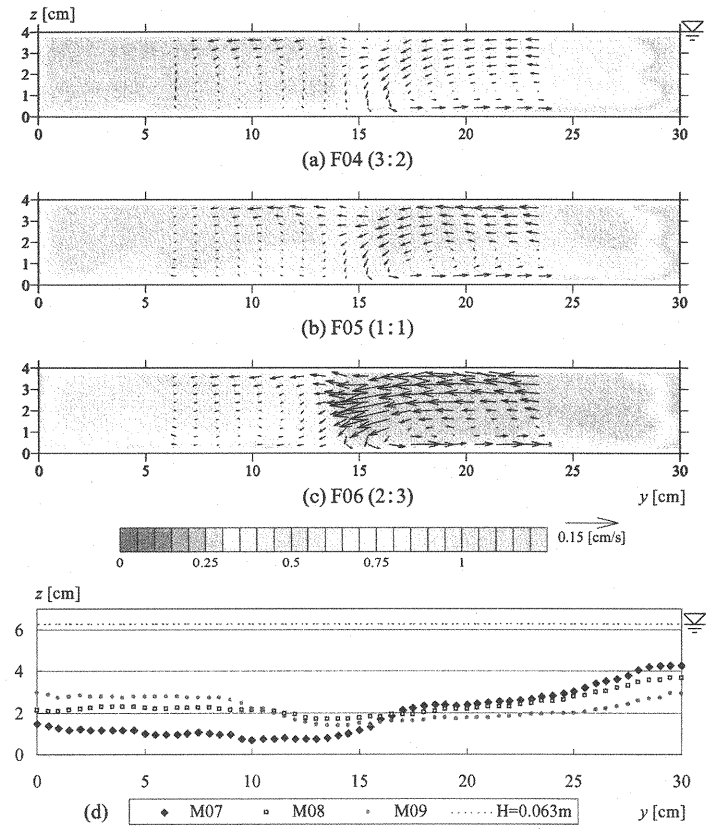


Fig.12 Comparison of secondary flow pattern in fixed bed and bathymetry of movable bed at $x$=15cm

line as shown in Fig.13(a). The secondary flows induce a downward flow towards the bottom, which inhibits the sand particles from entering the wedge-like zone from upstream, while locally scours the bottom in non-equilibrium condition as illustrated in Fig.13(b). Therefore, trajectories of bed load particles are deflected passing around the scouring zone and the scouring process proceeds until it reaches a critical condition of static equilibrium. During the above process, part of the sediment scoured from the zone is accumulated on the downstream of the tributary channel due to the transverse pressure gradient. The final stage of the bed variation is illustrated in Fig.13(c). At this stage, a static equilibrium zone with longitudinal scour hole and dynamic equilibrium zones on its side coexist within the confluence region. With respect to the development of scour hole, the cross-sectional shape at the line segment A-A' depicted in Fig13 evolves from a flat bed to the complicated bed shape subject to scouring and deposition of sediment particles. The equilibrium zones extend

into a downstream direction and finally reach a dynamic equilibrium with a horizontal bed in a far downstream region.

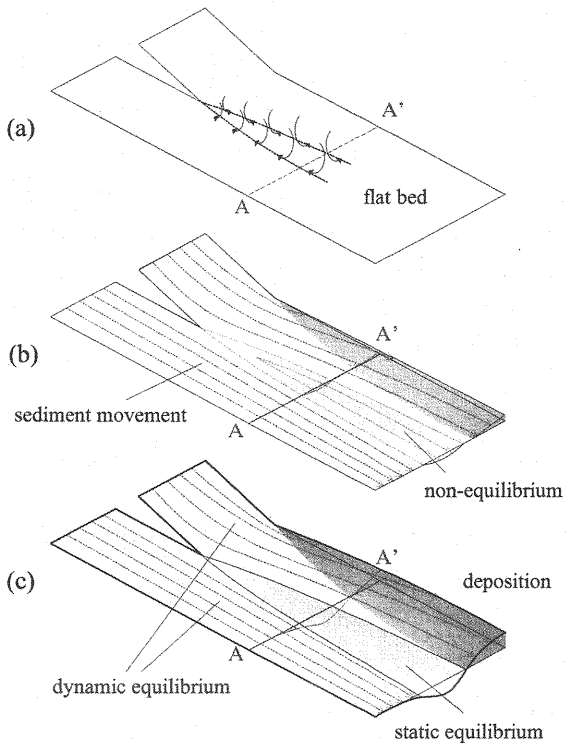


Fig.13 Schematic diagram of local scour development at a confluence

## CONCLUSIONS

In the present research, fixed bed and movable bed experiments at a confluence with a relatively small angle of 15 degrees are carried out to examine the genuine influence of the combining flows without any contraction or expansion of the channel by eliminating the effect of large-scale vortices downstream of the junction point usually observed in large-angled confluence flow. In the fixed bed experiment, detailed PIV measurements revealed the generation of a pair of secondary flows along the dividing line between the two combining flows even for a relatively small confluence angle. The significant characteristics detected in the experiment is that the center of the secondary flow was located not in the middle but closer to the bed. The secondary flow thus generated became a driving force to the local scour at the confluence in the case of movable bed experiments. Furthermore, from the observation of bottom particle movements, a general process of bed variation at a small-angled confluence is proposed, in which dynamic and static equilibrium conditions coexist. Such bed variations produced by secondary flows are difficult to reproduce in a two-dimensional simulation based on shallow water equations. Hence, a new bed shear stress model which takes into account the effects of secondary flow has to be developed to simulate a bed variation of confluence flow. The experimental results obtained in

the present research could provide significant data for evaluating two or three dimensional numerical simulations.

## REFERENCES


1. Weerakoon, S. B. and Tamai, N.: Three-dimensional calculation of flow in river confluences using boundary fitted coordinates, Journal of Hydroscience and Hydraulic Engineering, 7, pp.51-62, 1989.
2. Fujita, I. and Komura, S.: Three-dimensional structure of the flow at an open-channel confluence, Annual Journal of Hydraulic Engineering, Japan Society of Civil Engineers, 34, pp.301-306, 1990 (in Japanese).
3. Fujita, I. and Komura, S.: Analysis of the flow at a confluence by a discrete vortex method, Journal of Hydraulic, Coastal and Environmental Engineering, Japan Society of Civil Engineers, 411/II-12, pp.25-33, 1989 (in Japanese).
4. Fujita, I., Komura, S. and Wada, K.: Analysis of surface-flow patterns at a right-angled open-channel confluence, Annual Journal of Hydraulic Engineering, Japan Society of Civil Engineers, 34, pp.713-718, 1990 (in Japanese).
5. Cheng, L., Komura, S. and Fujita, I.: Numerical simulation of the confluence flow by k-ε models, Annual Journal of Hydraulic Engineering, Japan Society of Civil Engineers, 36, pp.169-174, 1992.
6. Fujita, I. and Komura, S.: Investigation of large-scale separated eddies at a confluence by using image processing technique, Annual Journal of Hydraulic Engineering, Japan Society of Civil Engineers, 36, pp.187-192, 1992 (in Japanese).
7. Weerakoon, S. B. and Tamai, N.: Three-dimensional calculation of flow in river confluence using boundary-fitted coordinates, Journal of Hydroscience and Hydraulic Engineering, 7, pp.51–62, 1989.
8. Bradbrook, K. F., Lane, S. N. and Richards, K.S.: Numerical simulation of time-averaged flow structure at river channel confluences, Water Resources Research, 36, 2731-2746, 2000.
9. Miyawaki, S., Constantinescu, G., Kirkil, G., Rhoads, B. and Sukhodolov, A.: Numerical Investigation of Three-Dimensional Flow Structure at a River Confluence, 33rd IAHR Congress, 2009.
10. Kadotani, K., Tanaka, T. and Fujita, I.: Three dimensional feature of open-channel confluence flow with small junction angle, Annual Journal of Hydraulic Engineering, Vol.53, pp.925-930, 2009 (in Japanese).
11. Werner, H. and Wengle, H.: Large-eddy simulation of turbulent flow over and around a cube in a plane channel, Turbulent Shear Flow 8, pp.155-168, Springer-Verlag, Berlin, 1991.


## APPENDIX - NOTATION

The following symbols are used in this paper:

$_1$ = stands for parameters in the upstream main channel,

$_2$ = stands for parameters in the tributary channel,

$_3$ = stands for parameters in the downstream main channel,

$B$ = channel width;

$Fr$ = the Froude number;

$h$ = water depth;

$Q$ = discharge;

$Qr$ = discharge ratio defined by $Q_2/Q_3$;

$Re$ = Reynolds number;

$u$ = mean velocity in $x$-axis;

$u_*$ = friction velocity in $x$-axis;

$v$ = mean velocity in $y$-axis;

$v_*$ = friction velocity in $y$-axis;

$w$ = mean velocity in $z$-axis;

$x$ =streamwise coordinate;

$y$ = lateral coordinate;

$z$ = vertical coordinate from the channel bed.

(Received Aug, 01, 2010 ; revised Mar, 22, 2011)